Faraday Discussions

Cite this: *Faraday Discuss.*, 2015, **182**, 457

PAPER

Chromium deposition and poisoning of $La_{0.8}Sr_{0.2}MnO_3$ oxygen electrodes of solid oxide electrolysis cells

Kongfa Chen,[a] Junji Hyodo,[b] Aaron Dodd,[c] Na Ai,[a] Tatsumi Ishihara,[bd] Li Jian[e] and San Ping Jiang*[a]

Received 25th January 2015, Accepted 2nd March 2015
DOI: 10.1039/c5fd00010f

The effect of the presence of an Fe–Cr alloy metallic interconnect on the performance and stability of $La_{0.8}Sr_{0.2}MnO_3$ (LSM) oxygen electrodes is studied for the first time under solid oxide electrolysis cell (SOEC) operating conditions at 800 °C. The presence of the Fe–Cr interconnect accelerates the degradation and delamination processes of the LSM oxygen electrodes. The disintegration of LSM particles and the formation of nanoparticles at the electrode/electrolyte interface are much faster as compared to that in the absence of the interconnect. Cr deposition occurs in the bulk of the LSM oxygen electrode with a high intensity on the YSZ electrolyte surface and on the LSM electrode inner surface close to the electrode/electrolyte interface. SIMS, GI-XRD, EDS and XPS analyses clearly identify the deposition and formation of chromium oxides and strontium chromate on both the electrolyte surface and electrode inner surface. The anodic polarization promotes the surface segregation of SrO and depresses the generation of manganese species such as Mn^{2+}. This is evidently supported by the observation of the deposition of $SrCrO_4$, rather than $(Cr,Mn)_3O_4$ spinels as in the case under the operating conditions of solid oxide fuel cells. The present results demonstrate that the Cr deposition is essentially a chemical process, initiated by the nucleation and grain growth reaction between the gaseous Cr species and segregated SrO on LSM oxygen electrodes under SOEC operating conditions.

[a]*Fuels and Energy Technology Institute, Department of Chemical Engineering, Curtin University, Perth, WA 6102, Australia. E-mail: s.jiang@curtin.edu.au; Fax: +61 8 9266 1138; Tel: +61 8 9266 9804*

[b]*Department of Applied Chemistry, Faculty of Engineering, Kyushu University, Motooka 744, Nishi-ku, Fukuoka, 819-0395, Japan*

[c]*Centre for Microscopy, Characterisation and Analysis, The University of Western Australia, WA 6009, Australia*

[d]*International Institute for Carbon-Neutral Energy Research (WPI-I2CNER), Kyushu University, Motooka 744, Nishi-ku, Fukuoka, 819-0395, Japan*

[e]*Center for Fuel Cell Innovation, School of Materials Science and Engineering, State Key Laboratory of Material Processing and Die & Mould Technology, Huazhong University of Science and Technology, Wuhan 430074, China*

1. Introduction

Solid oxide electrolysis cells or solid oxide electrolyzers (SOECs or SOEs) operating at high temperatures of 700–1000 °C are highly efficient to store the electrical energy generated by renewable sources such as solar and wind power into chemical energy of fuels such as hydrogen, syngas and methane. SOECs are reversible solid oxide fuel cells (SOFCs), and state-of-the-art SOFC materials such as nickel-based cermets, yttria-stabilized zirconia (YSZ) electrolyte and lanthanum strontium manganite (LSM) perovskites can be directly applied as electrode and electrolyte materials in SOECs.

A major issue for the development of SOECs is the significant performance degradation during long-term operation,[1,2] and the decay of oxygen electrodes has been regarded as the major cause, particularly at high currents.[3,4] The degradation of oxygen electrodes has been extensively studied and several degradation/failure modes of the oxygen electrodes have been proposed. The most common mode of failure is the occurrence of delamination at the oxygen electrode/electrolyte interface,[5–7] and it is generally believed that the main reason is the buildup of high internal oxygen pressure within the electrolyte close to the oxygen electrode/electrolyte interface.[8,9] On the other hand, Kim *et al.* suggested that the densification of porous LSM–YSZ oxygen electrodes caused by cation migration at a high anodic current is responsible for the complete delamination of oxygen electrodes.[10] Keane *et al.* proposed that the formation of highly resistive $La_2Zr_2O_7$ at the electrode/electrolyte interface is attributed to the LSM electrode delamination.[11] Our studies have shown that the delamination of LSM oxygen electrodes is mainly due to the disintegration or breaking of LSM particles and formation of nanoparticles at the electrode/electrolyte interface.[12,13] The formation of nanoparticles at the electrode/electrolyte interface is most likely caused by the LSM lattice shrinkage and thereby formation of local tensile strains due to the forced oxygen ion migration from the electrolyte into the LSM grains under the anodic polarization potential driving force.[13] For the (La,Sr) $(Co,Fe)O_3$ (LSCF) oxygen electrodes after the electrolysis test for 9000 h, the perovskite structure is partly demixed, accompanied by microstructure change and formation of Co_3O_4; and a dense $SrZrO_3$ layer is also observed at the Gd-doped ceria (GDC) interlayer/YSZ electrolyte interface.[14,15] Separation of GDC interlayer from the YSZ electrolyte has also been reported.[16,17]

A chromia-forming stainless steel alloy is the leading interconnect material for planar SOFCs due to its ease of fabrication, high thermal and electrical conductivity and low cost.[18] However, volatile Cr species such as CrO_3 and $CrO_2(OH)_2$ from the Cr_2O_3 protective scale on the metallic interconnect, deposit and poison the electrochemical activity and stability of LSM electrodes under SOFC operating conditions.[19] It is well known that the LSM electrodes are vulnerable to attack by chromium, forming products such as Cr_2O_3 and $(Cr,Mn)_3O_4$ spinel primarily at the electrode/electrolyte interface region and on the electrolyte surface under the cathodic polarization conditions.[20–22] Similar to that of SOFCs, Fe–Cr alloys are also commonly used as interconnect materials for SOECs.[23] Very different from the large amount of literature on Cr deposition and poisoning of SOFC cathodes,[19,24] studies on Cr poisoning and deposition on SOEC oxygen electrodes are very rare. Our early study on Cr poisoning of LSM electrodes showed that under

anodic polarization at 200 mA cm^{-2} and 900 °C, fine grains of chromium oxide are deposited on the YSZ electrolyte surface.[21] Most recently, we studied Cr deposition and poisoning of LSCF oxygen electrodes of SOECs and showed that the deposition of chromium species such as $SrCrO_4$, Cr_2O_3 and Cr_2O_5 is preferential at the outermost surface of the LSCF electrodes, leading to a substantial increase of electrode polarization and ohmic resistances.[25] For a bi-layered oxygen electrode consisting of a (La,Sr)CoO_3 (LSC) contact layer, Cr deposition occurred throughout the whole LSC contact layer after polarization under SOEC conditions for 2000 h and transportation of Sr and Co cations to the electrode's outermost surface and formation of La–Cr–O phases were observed.[26] However, Cr deposition and interaction with oxygen electrodes such as LSM is largely unknown under SOEC conditions despite the significance of LSM in the development of SOEC technologies.

In this paper, the activity and stability of LSM oxygen electrodes is studied for the first time under SOEC operating conditions in the presence of an Fe–Cr interconnect. The results show the deposition of Cr species at the electrode/electrolyte interface under SOEC operating conditions and the presence of Cr species accelerates the degradation and delamination of LSM oxygen electrodes.

2. Experimental

Stoichiometric $La_{0.8}Sr_{0.2}MnO_3$ (LSM, Fuel Cell Materials, USA) oxygen electrodes were prepared on 0.18 mm thick dense YSZ wafers (Huazhong University of Science and Technology, China) by slurry coating, and sintered at 1150 °C for 3 h. The thickness of the LSM coating was 15–30 μm and the electrode surface area was 0.5 cm^2. Electrochemical measurements of LSM oxygen electrodes were carried out in a three-electrode configuration,[27] using a Gamry ref. 3000 Potentiostat. Chromia-forming alloy (RA446, 23–27% Cr, Rolled Alloy Co.) was used as the Fe–Cr interconnect in this study. Alloys were machined into coupons (12 mm × 12 mm × 5 mm thick). One side of the coupon was cut with channels (1.2 mm × 1.2 mm deep) with holes in the center. Air (industrial grade) was distributed to the electrode surface through channels by an alumina tube, simulating the air flow situation in an actual cell stack of planar-type SOEC. Two Pt wires were spot-welded to the coupon to serve as voltage and current probes, respectively. There was no additional Pt mesh placed between the chromia-forming alloy and the LSM electrode. In this arrangement, the chromia-forming alloy also acted as the current collector. The configuration for the arrangement of the electrode and interconnect is similar to that used in the SOFC studies.[21]

Electrochemical behavior of LSM oxygen electrodes was studied at 200 and 500 mA cm^{-2} and 800 °C with an air flow rate of 100 ml min^{-1}. Electrochemical impedance curves were measured under open circuit with frequency range from 0.1 Hz to 100 kHz and the signal amplitude of 10 mV. Electrode polarization resistance, R_E was measured by the differences between the high and low frequency intercepts, and electrode ohmic resistance, R_Ω was obtained from the high frequency intercept. For comparison, the electrochemical performance of LSM oxygen electrodes was also measured in the absence of Fe–Cr interconnect. In this case Pt mesh was used as the current collector. To confirm the reproducibility, at least two samples were tested under the same conditions.

The microstructure of the electrodes was examined using scanning electron microscopy (SEM, Zeiss Neon 40EsB) equipped with X-ray energy dispersion spectroscopy (EDS). In some cases, the electrodes after the electrochemical tests were removed by treatment in 3M HCl solution. Element imaging and line scan profiles on the polished cross sections were conducted using time of flight secondary ion mass spectroscopy (TOF.SIMS, ionToF, Germany) in the imaging mode with a 30 keV Bi^+ beam, a spot size of *ca.* 150 nm, and a raster size of 100 μm × 100 μm. Before the measurement, the cross-section was sputtered with 2 keV Ar^+ to remove polishing residues and adsorbed molecules on the sample surface. The phase of the YSZ electrolyte surface after the electrode delamination and/or after the acid treatment was characterized by a grazing incidence X-ray diffractometry (GI-XRD, Panalytical Empyrean XRD) with Cu K_α radiation at a step size of 0.005° and step time of 2.5 s. X-ray photoelectron spectroscopy (XPS) was carried out using a Kratos AXIS Ultra DLD system, with monochromated Al K_α X-rays (photon energy 1486.7 eV), a 700 μm × 300 μm aperture and a pass energy of 40 eV. The XPS spectra were calibrated with the C1s peak at 284.8 eV.

3. Results

3.1. Electrochemical performance

Fig. 1 shows the polarization curves of LSM oxygen electrodes under anodic currents of 200 and 500 mA cm^{-2} for 20 h in the absence and presence of an Fe–Cr interconnect. For the reaction under a low current of 200 mA cm^{-2}, R_E changes

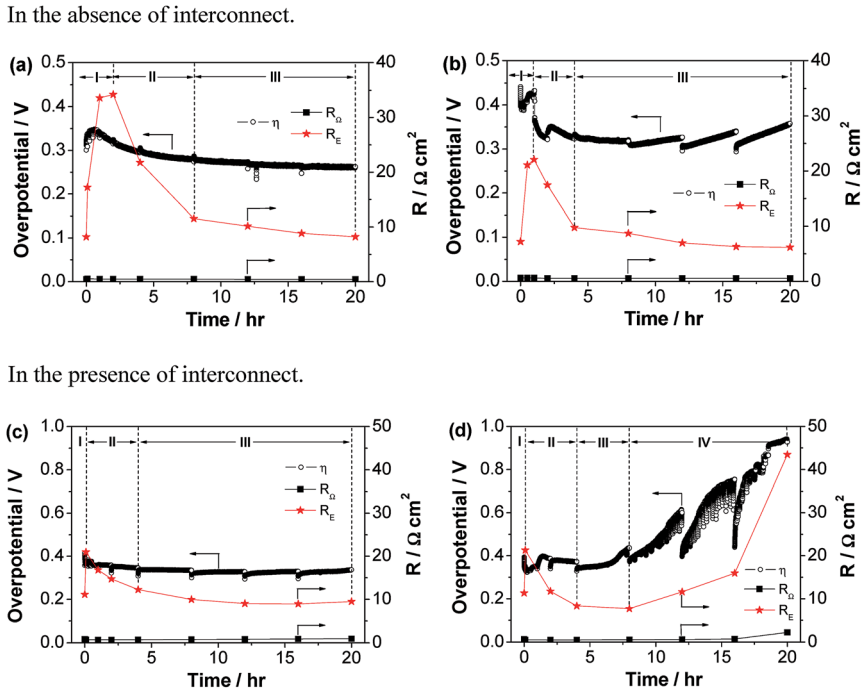

Fig. 1 Polarization curves of LSM oxygen electrodes as a function of anodic current passage time at (a,c) 200 mA cm^{-2} and (b,d) 500 mA cm^{-2}, 800 °C for 20 h in (a,b) the absence and (c,d) presence of Fe–Cr interconnect.

significantly with anodic polarization, showing three distinctive stages (Fig. 1a). R_E increases rapidly from 8.2 Ω cm^2 initially to 34.2 Ω cm^2 after anodic polarization for 2 h (stage I), then decreases rapidly to 11.5 Ω cm^2 after being polarized for 8 h (stage II). The decrease becomes much slower with further polarization (stage III). After anodic polarization for 20 h, R_E reaches 8.2 Ω cm^2, almost the same as the initial value. This indicates the initial activity decay of LSM electrode is recoverable by extended anodic polarization time. In the case of polarization at a high current of 500 mA cm^{-2} (Fig. 1b), R_E follows a similar trend of changes with three stages, but the change of R_E occurs faster under the higher current *e.g.* the duration of stages I and II is 1 and 3 h, respectively, significantly shorter than 2 and 6 h of the same stages in the case of the low currents. R_Ω is very stable during the test, and no delamination was observed after polarization at 200 and 500 mA cm^{-2}.

The polarization behavior of LSM oxygen electrodes in the presence of the Fe–Cr interconnect also shows three distinctive polarization regions (Fig. 1c). For the reaction in the presence of the interconnect, the initial R_E is ~11 Ω cm^2 and increases to 20.1 Ω cm^2 after being polarized for 5 min (stage I), followed by a rapid decrease to 12 Ω cm^2 after being polarized for 4 h (stage II), and stabilized at

In the absence of interconnect.

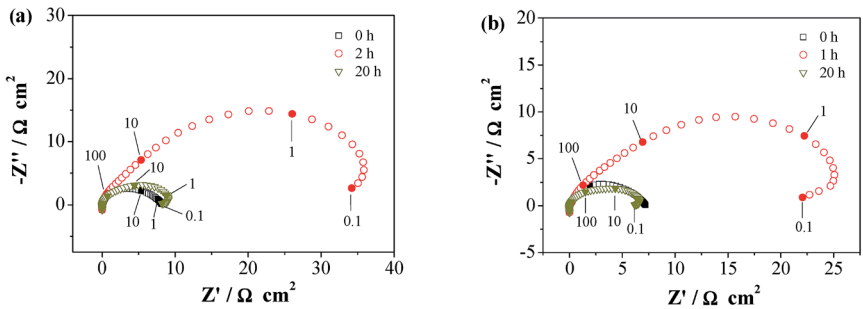

In the presence of interconnect.

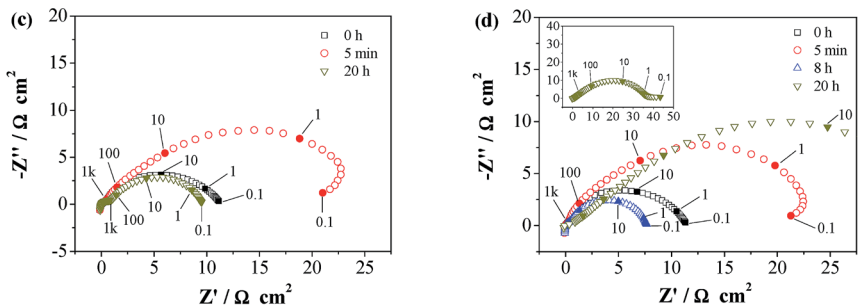

Fig. 2 Electrochemical impedance curves of LSM oxygen electrodes as a function of anodic current passage time at (a,c) 200 mA cm^{-2} and (b,d) 500 mA cm^{-2}, 800 °C for 20 h in (a,b) the absence and (c,d) presence of Fe–Cr interconnect. The high frequency intercepts of the EIS curves were adjusted to zero for the purpose of clarity.

9.5 Ω cm^2 after being polarized for 20 h (stage III). Compared to the reaction in the absence of the interconnect (Fig. 1a), the duration of stage I and II of the LSM oxygen electrodes in the presence of the interconnect is shortened. In the case of polarization under a high current of 500 mA cm^{-2} (Fig. 1d), the period for stage III is substantially reduced (*i.e.*, 4 h), followed by a dramatic increase of R_E from 7.7 Ω cm^2 to 43.5 Ω cm^2 after polarization treatment for 20 h. This is very different from that observed in the absence of the Fe–Cr interconnect, R_Ω also increases substantially from 0.68 Ω cm^2 initially to 2.26 Ω cm^2 at the end of the experiment. Complete delamination of the LSM electrode was observed after polarization for 20 h, much shorter than 48 h observed in the absence of the interconnect under similar testing conditions.[13] The results clearly indicate that gaseous Cr species poisoned and degraded the electrocatalytic activity of LSM oxygen electrodes under SOEC operating conditions.

Fig. 2 shows the impedance responses of LSM oxygen electrodes during anodic polarization in the absence and presence of the Fe–Cr interconnect. The initial impedance responses of the LSM electrode in the absence of the interconnect are characterized by a large depressed arc (Fig. 2a). The impedance arcs (*i.e.*, R_E) increase significantly after anodic polarization at 200 mA cm^{-2} for 2 h, but decrease substantially after polarization for 20 h, and the change is mainly on the low frequency arc. Similar impedance behavior was also observed for the reaction under a high current of 500 mA cm^{-2} (Fig. 2b). During the anodic polarization at 200 mA cm^{-2} in the presence of the interconnect (Fig. 2b), the change in low frequency arcs follows similar patterns to that in the absence of the interconnect, though the initial increase occurs in a much shorter period. Under a high current of 500 mA cm^{-2}, the size of the impedance arc increases after being polarized for 5 min and decreases again after polarization for 8 h (Fig. 2d). On the other hand, R_E increased significantly to 43.5 Ω cm^2 after being polarized for 20 h, much higher than 11.3 Ω cm^2 measured on the LSM oxygen electrode before polarization. The substantial increase in the R_E indicates the poor interfacial contact between the LSM electrode and YSZ electrolyte, consistent with the significant activity loss of the LSM oxygen electrode as shown in Fig. 1d.

3.2. Microstructure

Fig. 3 shows the SEM micrographs of the YSZ electrolyte surface and LSM electrode surface in contact with YSZ electrolyte (*i.e.* the inner surface). The LSM electrodes after anodic polarization at 200 and 500 mA cm^{-2} for 20 h in the absence of Fe–Cr interconnect were removed by adhesive tape. There are contact rings on the YSZ electrolyte surface formed during the electrode sintering process due to the cation inter-diffusion between the LSM electrode and YSZ electrolyte.[28,29] Due to the forced separation, there are residue particles located in ring-shaped regions on the electrolyte surface (Fig. 3a and c) and the electrolyte surface areas between the contact rings are clean. For polarization at the lower current of 200 mA cm^{-2}, there are nanoparticles in the size range of 30–70 nm within the contact ring areas (indicated by arrows, Fig. 3a) and irregularly shaped larger residue particles. The existence of nanoparticles indicates the disintegration of LSM particles under SOEC anodic polarization conditions.[13] The irregularly shaped residue particles have an identical morphology observed on the inner surface of LSM electrode (Fig. 3b and d), indicating that LSM electrodes are still in

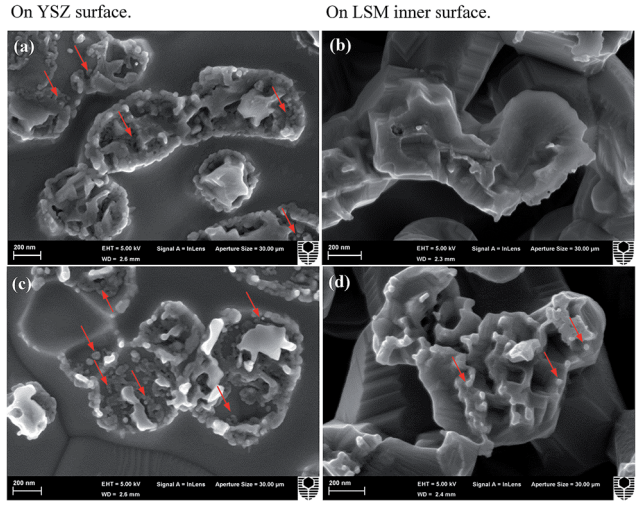

Fig. 3 SEM micrographs of the YSZ surface (left) and LSM inner surface (right) at the electrolyte/electrode interface region for an LSM oxygen electrode after anodic polarization at (a,b) 200 mA cm^{-2} and (c,d) 500 mA cm^{-2}, 800 °C for 20 h in the absence of the interconnect. The LSM electrode was removed by adhesive tape. Arrows indicate the nanoparticles formed.

intimate contact with the YSZ electrolyte. In the case of LSM electrode after being polarized at a high current of 500 mA cm^{-2}, the formation of nanoparticles is more pronounced and there are also fewer nanoparticles formed on the LSM electrode inner surface (Fig. 3b and d). This indicates that the disintegration of LSM particles and nanoparticle formation processes are much faster under a high current, which is consistent with electrochemical polarization results (Fig. 1).

Fig. 4 shows the SEM micrographs of the YSZ electrolyte surface and LSM electrode inner surface after anodic polarization at 200 mA cm^{-2} for 20 h in the presence of the Fe–Cr interconnect. The LSM oxygen electrode coating was removed by an adhesive tape. It was found that the electrode coatings in direct contact with the rib of the interconnect can be easily removed, while the coatings under the channel of the interconnect still adhered to the electrolyte (Fig. 4g). For the YSZ surface under the rib of the interconnect, the electrolyte surface between the contact rings is no longer clean, and is covered by deposits with a size range of 50–200 nm (Fig. 4a). The contact rings are occupied by a large number of nanoparticles in the size of 20–30 nm (indicated by arrows, Fig. 4c), and a few larger irregularly shaped residue particles. Such nanoparticles were also observed on the electrode inner surface (indicated by arrows, Fig. 4e). On the LSM inner surface there are also formations of particles with very different crystal facets and morphology to the LSM particles (circled in Fig. 4e). In the case of the electrolyte surface under the channel of the interconnect, the electrolyte surface between the rings is also covered by deposits (Fig. 4b). However, no nanoparticles were observed either in the contact rings or on the electrode inner surface (Fig. 4d and f). Instead there are large particles with a feature of forced fracture in the rings (Fig. 4b and d), indicating that LSM particles under the channels of the interconnect are intact with negligible disintegration. The significant nanoparticle formation under

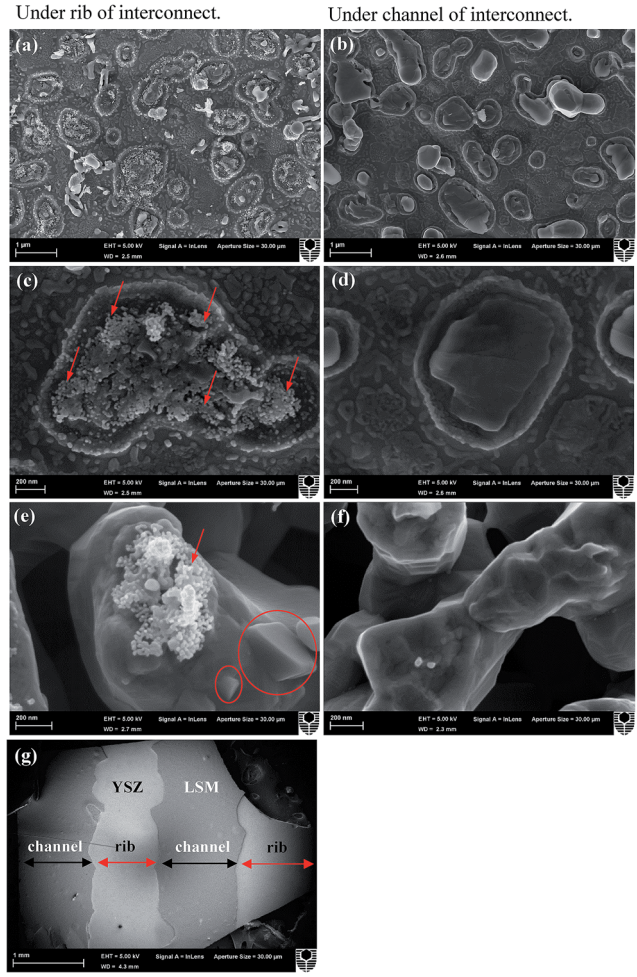

Fig. 4 SEM micrographs of the electrolyte/electrode interfaces under the rib (left) and channel (right) of the Fe–Cr interconnect, for a LSM oxygen electrode after anodic polarization at 200 mA cm^{-2}, 800 °C for 20 h: (a–d) the YSZ electrolyte surface, and (e, f) the LSM inner surface in contact with the YSZ electrolyte. Overview of the surface of the electrode partly removed by adhesive tape is shown in (g).

the rib of the interconnect as compared to that under the channel of the interconnect implies that the LSM electrode in direct contact with the interconnect is the major reaction site for the oxygen evolution reaction due to the much shorter current transfer pathway, thus giving rise to the preferential disintegration of LSM particles and occurrence of delamination of the portion of the LSM electrode under the rib of the interconnect (Fig. 4c and g).

Fig. 5 shows the SEM micrographs and EDS profiles of the YSZ electrolyte surface and LSM electrode surface under the rib of the interconnect, after anodic polarization at a high current of 500 mA cm^{-2} for 20 h. Similar to that observed on LSM electrodes polarized under a low current of 200 mA cm^{-2}, there are nanoparticles formed in the contact rings on the YSZ surface and on the LSM inner

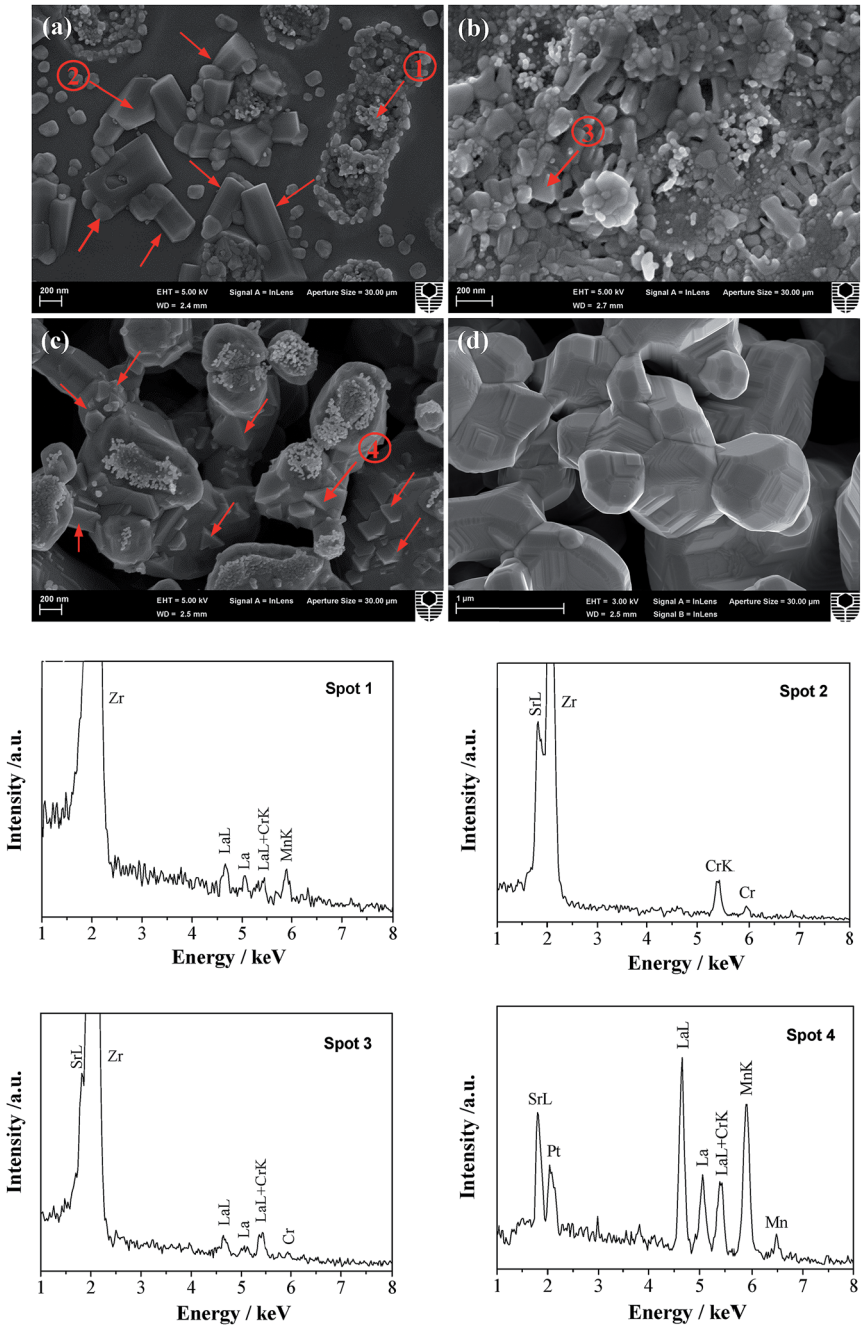

Fig. 5 SEM micrographs and spot EDS profiles of (a,b) the YSZ electrolyte surface and (c) the LSM inner surface and (d) the LSM outermost surface under the rib of the Fe–Cr interconnect after anodic polarization at 500 mA cm^{-2}, 800 °C for 20 h. The LSM electrode was delaminated after the test.

Table 1 Relative EDS peak intensity ratios of the selected areas as shown in Fig. 5

Locations	$Sr_{L\alpha}/La_{L\alpha}$	$(La_{L\beta2}+Cr_{L\alpha})/La_{L\alpha}$	$Mn_{K\alpha}/La_{L\alpha}$
As-prepared LSM surface	0.84	0.22	0.60
Spot 1, Fig. 5a	—	0.74	0.90
Spot 2, Fig. 5a	—	—	—
Spot 3, Fig. 5b	5.58	0.94	—
Spot 4, Fig. 5c	0.74	0.41	0.78

surface (Fig. 5a and c). Different from the numerous and fine nanoparticles formed on the electrolyte surface under a low current of 200 mA cm^{-2} (Fig. 4a), the deposits are large in size (200–800 nm) and have characteristics of octahedral crystal facets (indicated by allows, Fig. 5a). Such particles in the size range of 120–400 nm were also observed on the LSM inner surface (indicated by arrows, Fig. 5c). In some areas, the deposits were a mixture of nanoparticles and particles with clear crystal facets (Fig. 5b). On the other hand, the outermost surface of LSM oxygen electrode is clean and there is no deposition or formation of deposits after polarization at 500 mA cm^{-2} for 20 h (Fig. 5d).

EDS analysis was conducted on selected particles on the YSZ electrolyte surface and on the LSM inner surface (indicated by numbers 1 to 4, see Fig. 5), and the ratios of peak intensity are listed in Table 1. For comparison, EDS was also performed on the as-prepared LSM electrode. As $La_{L\beta2}$ and $Cr_{L\alpha}$ peaks are superimposed at ~5.88 keV, the ratio of $(La_{L\beta2}+Cr_{L\alpha})/La_{L\alpha}$ compared to that of $La_{L\beta2}/La_{L\alpha}$ of the as-prepared LSM is an indication of Cr deposition.[30] For the nanoparticles within the contact rings (spot 1, Fig. 5a), $(La_{L\beta2}+Cr_{L\alpha})/La_{L\alpha}$ is 0.74, significantly higher than 0.22 of the as-prepared LSM, indicating Cr deposition in the contact rings. The $Mn_{K\alpha}/La_{L\alpha}$ ratio is 0.90, slightly higher than 0.60 of the as-prepared LSM. This may suggest the decomposition of LSM with the formation of manganese oxides. In the case of the large deposits with octahedral facets on the YSZ surface (spot 2, Fig. 5a), the observation of distinct Sr and Cr peaks with negligible Mn signal indicates the possible formation of the $SrCrO_4$ phase. The deposits formed on different parts of the YSZ electrolyte surface (spot 3, Fig. 5b) contain La, Sr and Cr and could also be related to thermodynamically stable $SrCrO_4$ phase. For the deposits on the LSM inner surface (spot 4, Fig. 5c), the $(La_{L\beta2}+Cr_{L\alpha})/La_{L\alpha}$ is 0.41, also significantly higher than 0.22 of the as-prepared LSM, indicating the formation of chromium oxides and/or $SrCrO_4$. The $Mn_{K\alpha}/La_{L\alpha}$ ratio is 0.78, close to 0.60 of the as-prepared LSM, indicating that Mn is most likely in the LSM perovskite structure in this case.

Fig. 6 shows the SEM micrographs of the YSZ electrolyte surface and LSM electrode inner surface under the channel of the interconnect after anodic polarization at a high current of 500 mA cm^{-2} for 20 h. On the electrolyte surface areas between the contact rings (Fig. 6a), there are deposits with clear crystal facets but the amount is much lower compared to under the rib of the interconnect (Fig. 5). There are formations of relatively large nanoparticles in the range of 60–100 nm (Fig. 6b) and closely packed fine nanoparticles in the range of 30–60 nm (Fig. 6c). After acid treatment, the electrolyte surface becomes clean with distinctively visible contact rings (Fig. 6d). The electrode inner surface is

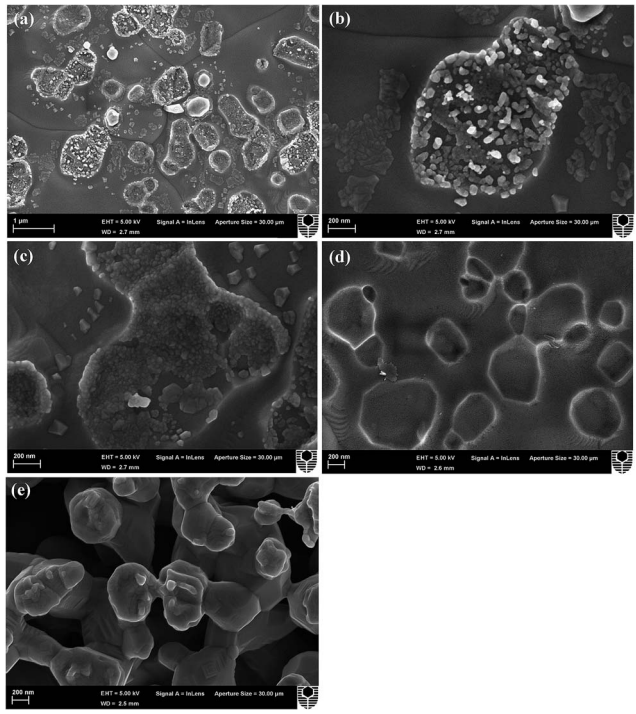

Fig. 6 SEM micrographs of the YSZ electrolyte surface and LSM inner surface under the channel of the Fe–Cr interconnect after anodic polarization at 500 mA cm^{-2}, 800 °C for 20 h: (a–c) YSZ surface before acid treatment, (d) YSZ surface after acid treatment, (e) LSM electrode inner surface in contact with the electrolyte. The LSM electrode was delaminated after the test.

generally clean with few fine particles (Fig. 6e). The deposition and formation of Cr particles on the YSZ electrolyte surface and LSM inner surface under the channel of the interconnect are much less, as compared to that under the rib of the interconnect, similar to that observed on the LSM electrode polarized under a low current of 200 mA cm^{-2} (Fig. 4).

3.3. Cr distribution and phase analysis

Fig. 7 shows the SIMS imaging and line scan profiles on the polished LSM electrode/YSZ electrolyte interfaces under the rib of the Fe–Cr interconnect after anodic polarization at 500 mA cm^{-2} for 1 and 8 h. In both cases, the SIMS image indicates chromium deposition along the entire electrode bulk (Fig. 7a and b). The line scan profiles show significantly higher deposition of chromium at the electrode/electrolyte interface region as compared to that in the bulk (Fig. 7c and d).

Fig. 8 shows the GI-XRD patterns of the YSZ electrolyte surface before and after anodic polarization at 800 °C. GI-XRD is a very sensitive technique used to probe the thin surface layer. For the as-prepared electrode, the electrode layer is removed by acid treatment, and there are typical YSZ diffraction peaks (PDF 04-001-9395) as well as minor $La_2Zr_2O_7$ peaks (PDF 00-017-0450) on the electrolyte

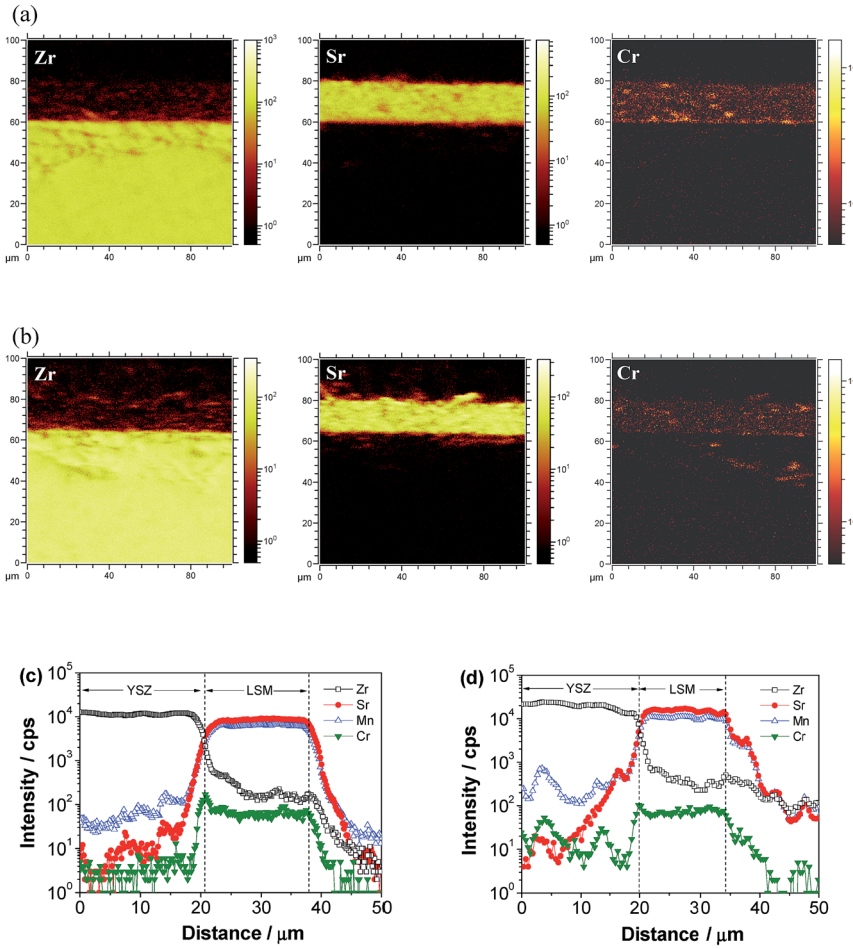

Fig. 7 SIMS imaging and line scan profiles on the cross section of the LSM oxygen electrodes under the rib of the Fe–Cr interconnect after anodic polarization at 500 mA cm^{-2}, 800 °C (a, c) for 1 h and (b, d) for 8 h.

surface (curve a, Fig. 8). The existence of minor $La_2Zr_2O_7$ phases indicates the chemical reaction between the LSM electrode and YSZ electrolyte during the electrode sintering process at 1150 °C.[31] After anodic polarization at 500 mA cm^{-2} for 48 h in the absence of the Fe–Cr interconnect, the entire electrode coating was peeled off of the electrolyte, and the LSM phase (PDF 04-015-1693) in addition to the $La_2Zr_2O_7$ phase (curve b, Fig. 8) was detected. The intensity of the LSM peak is substantially higher than that of the $La_2Zr_2O_7$ peak, indicating that the composition of the nanoparticles formed on the electrolyte surface after the electrode delamination (see Fig. 3c) is primarily LSM. This again confirms that nanoparticles formed within the contact rings originate from the disintegration or breaking of LSM particles with the LSM composition intact.[13] This is very different from the decomposition of LSM, as shown by Mizusaki *et al.*,[32] where LSM would decompose under low partial pressure of oxygen (*e.g.*, 10^{-18} atm at 800 °C),

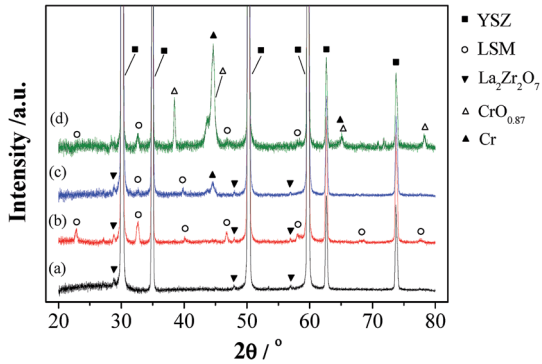

Fig. 8 GI-XRD patterns of the YSZ electrolyte surface in contact with the LSM oxygen electrodes (a) as-prepared electrode removed by acid treatment, and after the anodic current passage at 800 °C: (b) at 500 mA cm^{-2} for 48 h in the absence of the interconnect, (c) at 200 mA cm^{-2} for 20 h in the presence of Fe–Cr interconnect (prior to the measurement, the electrode was removed by acid treatment), and (d) at 500 mA cm^{-2} for 20 h in the presence of the Fe–Cr interconnect.

forming $La_{2-x}Sr_xMnO_4$, MnO and La_2O_3. After anodic polarization at 200 mA cm^{-2} for 20 h in the presence of the Fe–Cr interconnect and removal of the LSM electrode by acid treatment, there are Cr peaks (PDF 04-004-8467), $La_2Zr_2O_7$ peaks, and LSM peaks (curve c, Fig. 8). On the other hand, the LSM electrode was completely delaminated after anodic polarization at a high current

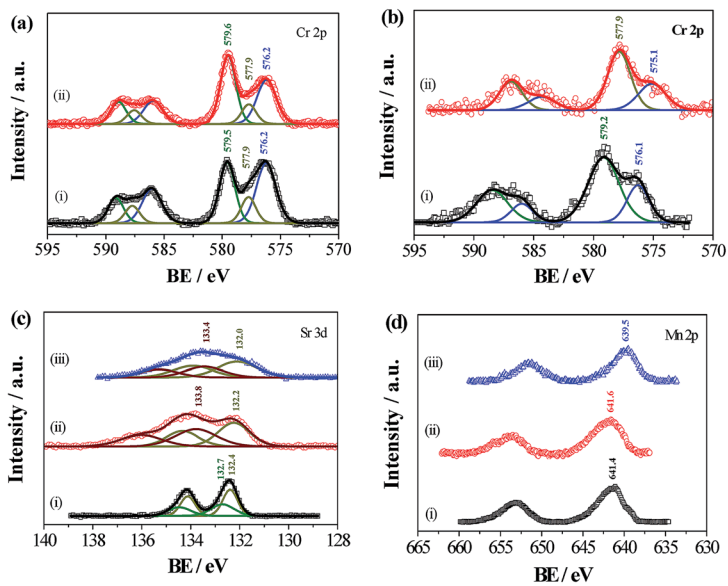

Fig. 9 XPS spectra of (a) Cr2p on the LSM electrode inner surface in contact with the YSZ electrolyte, (b) Cr2p, (c) Sr3d and (d) Mn2p on the YSZ electrolyte surface after anodic polarization at 500 mA cm^{-2} and 800 °C for 20 h in the presence of the Fe–Cr interconnect: (ii) under the channel and (iii) under the rib of the interconnect. The as-prepared LSM electrode surface is shown in (i).

of 500 mA cm^{-2} for 20 h in the presence of the Fe–Cr interconnect. In this case, Cr, $CrO_{0.87}$ (PDF 04-015-4940), and LSM phases were detected on the YSZ electrolyte surface (curve d, Fig. 8). GI-XRD results indicate $Cr/CrO_{0.87}$ deposition on the YSZ electrolyte surface for the LSM oxygen electrodes under SOEC operating conditions. However, the reason for the presence of metallic Cr is not clear at this stage.

Fig. 9 shows the XPS spectra conducted on the YSZ electrolyte surface and LSM electrode inner surface after anodic polarization at 500 mA cm^{-2} for 20 h in the presence of the Fe–Cr interconnect. On the LSM electrode inner surface (Fig. 9a), three distinctive $Cr2p_{3/2}$ peaks were observed at a low binding energy (BE) of 576.2 eV, medium BE of 577.7 eV and high BE of 579.5 eV, which are assigned to Cr_2O_3,[33] Cr_2O_5 [33] and $SrCrO_4$,[34,35] respectively. The Cr_2O_3, Cr_2O_5 and $SrCrO_4$ have a Cr ratio of 48.4%, 16.7% and 34.9% under the rib of the interconnect, and 40.9%, 15.3% and 43.8% under the channel of the interconnect, respectively. This indicates that the deposited Cr on the LSM inner surface is mainly in the form of Cr_2O_3 and $SrCrO_4$. On the electrolyte surface (Fig. 9b), there are only two $Cr2p_{3/2}$ peaks at a low BE of 576.1 eV related to Cr_2O_3 [33] and a high BE of 579.2 eV $SrCrO_4$ [34,35] under the channel of the interconnect, and at a low BE of 575.1 eV related to Cr_2O_3 [33] and at a medium BE of 577.9 eV related to Cr_2O_5 [33] under the rib of the interconnect. The Cr ratio is 32.5% for Cr_2O_3 and 67.5% for $SrCrO_4$ under the channel of the interconnect, and 35.4% for Cr_2O_3 and 64.6% for Cr_2O_5 under the rib of the interconnect, respectively. XPS results clearly show the formation of Cr_2O_3 and $SrCrO_4$ on both YSZ electrolyte surface and LSM electrode inner surface close to the interface.

The XPS spectra of Sr3d and Mn2p were also carried out on the electrolyte surface under the rib of the Fe–Cr interconnect after anodic polarization at 500 mA cm^{-2} for 20 h. For comparison, the outermost surface of an as-prepared LSM electrode was also characterized. On the as-prepared LSM electrode surface, two $Sr3d_{5/2}$ peaks appear at 132.4 and 132.7 eV (spectrum i, Fig. 9c), which are assigned to Sr in the LSM lattice (60%) and $SrCO_3$ on the LSM surface (40%),[36,37] respectively. After polarization in the presence of the interconnect, there is a significant change in the shape and peak position of the Sr3d spectra. The $Sr3d_{5/2}$ appears at a BE of 132.2 and 133.8 eV under the channel of the interconnect (spectrum ii, Fig. 9c), and at 132.0 and 133.4 eV under the rib of the interconnect (spectrum iii, Fig. 9c). The low BE peak at ~132 eV could be related to Sr in the bulk of LSM,[37,38] while the high BE peak at 133.4–133.8 eV may be associated with $SrCrO_4$.[38] This is based on the fact that in the literature, the BE of $Sr3d_{5/2}$ in SrO is

Table 2 Element ratios of the LSM inner surface and YSZ electrolyte surface after anodic polarization at 500 mA cm^{-2} for 20 h in the presence of Fe–Cr alloy interconnect

	Under rib		Under channel			
Elements	LSM inner surface/%	YSZ surface/%	LSM inner surface/%	YSZ surface/%	As-prepared LSM top surface/%	Stoichiometric $La_{0.8}Sr_{0.2}MnO_3$/%
La	46.4	44.6	39.6	47.8	47.8	40
Sr	6.8	8.5	13.2	8.5	8.1	10
Mn	33.6	36.5	33.1	31.0	44.1	50
Cr	13.2	10.4	14.1	12.7	0	0

135.0 eV,[39] significantly higher than a BE of 132.7 eV reported for $Sr3d_{5/2}$ in $SrCrO_4$.[38] In the case of the Mn2p XPS spectra, the $Mn2p_{3/2}$ peak occurs at 641.6 eV under the channel of the interconnect (spectrum ii, Fig. 9d), close to 641.4 eV of the as-prepared LSM electrode (spectrum i, Fig. 9d). This indicates the Mn valence state is between 3+ and 4+.[37,40] On the other hand, under the rib of the interconnect there is a shift of $Mn2p_{3/2}$ to a lower binding energy of 639.5 eV (spectrum iii, Fig. 9d), which suggests the presence of MnO.[41] This may indicate the partial decomposition of the LSM perovskite phase on the YSZ surface under the rib of the interconnect. Corresponding element ratios of LSM inner surface and YSZ electrolyte surface based on XPS analysis are given in Table 2.

4. Discussion

In the absence of the interconnect, the initial rapid increase in the electrode polarization resistance, R_E is most likely related to the deactivation effect of the anodic polarization on the electrocatalytic activity of LSM oxygen electrodes.[42,43] Our previous studies on the degradation and delamination of LSM oxygen electrodes have shown that the incorporation of oxygen ions from the electrolyte into the LSM grains under the anodic polarization potential driving force results in the shrinkage of the LSM lattice and thereby local tensile strains, leading to the microcracks and subsequent disintegration and breaking of LSM particles at the electrode/electrolyte interface.[12,13] The present study shows that the nanoparticles maintain the LSM phase and structure. The nanoparticle formation initially increases the three-phase boundaries (TPBs) and active surface areas for the oxygen oxidation reaction. This explains the rapid decrease in R_E in region II (Fig. 1a and b).

Similar polarization behavior was observed for the O_2 oxidation reaction in the presence of the Fe–Cr interconnect. However, the significantly reduced duration of the polarization changes in three regions and occurrence of the delamination at a high current of 500 mA cm^{-2} for the reaction in the presence of the Fe–Cr interconnect clearly demonstrate that the presence of the Fe–Cr interconnect poisons the electrocatalytic activity of the LSM oxygen electrode under SOEC operating conditions, similar to that reported for the LSM electrode under SOFC operating conditions.[44]

Very different from the preferential Cr deposition at the electrode/electrolyte interface region under SOFC operating conditions,[20–22,45] Cr deposition on the LSM oxygen electrode under SOEC operating conditions not only occurs on the YSZ electrolyte surface and at the electrode/electrolyte interface region but also in the LSM electrode bulk. The results indicate that the deposits with distinct crystal facets formed on the YSZ electrolyte surface between the contact rings and on the LSM electrode inner surface (see Fig. 5a and c) are most likely the $SrCrO_4$ phase and the small particles formed on the YSZ electrolyte surface within the contact rings and on LSM inner surface are a combination of Cr_2O_3 and Cr_2O_5. There is no evidence to indicate the formation of $(Cr,Mn)_3O_4$ spinels for the LSM oxygen electrodes under SOEC operating conditions. This is very different from the preferential Cr deposition at the electrode/electrolyte interface region and not in the electrode bulk, and the dominant formation of $(Cr,Mn)_3O_4$ spinels for the LSM electrodes under SOFC operating conditions.[20–22] However, such Cr deposition behavior of the LSM oxygen electrodes under SOEC operating conditions can

be explained by the accelerated surface segregation of SrO species under the anodic polarization conditions.

SrO surface segregation is known to occur on the as-prepared LSM electrodes.[46,47] One of the main driving forces for the Sr segregation is probably due to the fact that the cation dopant, Sr^{2+}, has a larger ionic radius than the host cation La^{3+}. The rather large Sr^{2+} is under a compressive strain/stress state in the bulk, which can be relaxed when it moves to the surface, resulting in the migration and formation of SrO species on the surface of related perovskites such as LSM and LSCF.[48–51] Yildiz *et al.* reported that the elastic energy caused by the size mismatch between Sr dopant and La host of LSM is the main driving force for the SrO surface segregation.[52] They also found that the SrO surface segregation increases at a high oxygen partial pressure, which causes lattice shrinkage of LSM and thereby an increase in dopant strain energy.[52] However, as shown by Fister *et al.*[53] the strain state has only a small impact on the Sr segregation for LSM thin films. This appears to be supported by the fact that under open circuit conditions, no Cr deposition or formation of $SrCrO_4$ is observed on the surface of LSM electrodes.[21]

In addition to the relation between the intrinsic compressive strain in the bulk and the Sr segregation, polarization appears to have a significant effect on the surface segregation of perovskites. Backhaus–Ricoult *et al.*[54] studied the LSM electrode/YSZ electrolyte interface using *in situ* photoelectron microscopy and observed the increased manganese segregation/migration under cathodic polarization at the interface. This implies that under anodic polarization conditions, manganese segregation would be depressed. Huber *et al.* studied *in situ* the surface segregation of $La_{0.75}Sr_{0.25}Cr_{0.5}Mn_{0.5}O_3$ under cathodic and anodic dc bias by XPS, and observed that cathodic polarization leads to the depletion of Sr on the LSCM surface while Sr surface segregation is promoted by anodic polarization.[55] Fig. 10a shows the scheme of the nanoparticle formation at the electrode/electrolyte interface and accelerated Sr segregation from the bulk to the surface under anodic polarization. As LSM is a predominant electronic conductor with negligible oxygen ion conductivity,[56] the O_2 evolution reaction would also occur primarily at the electrode/electrolyte contact and/or interface areas.[13] High anodic polarization potential at the electrode/electrolyte interface region would lead to the higher Sr segregation on LSM inner surface in the vicinities of the interface as compared to that in the electrode bulk.

It is well known that segregated SrO plays a critical role in the deposition and formation of $SrCrO_4$ on the LSCF surface in contact with a chromia-forming alloy under SOFC operating conditions.[19] In the case of LSM oxygen electrodes under SOEC operating conditions, Cr deposition would be dominated by the interaction between the gaseous Cr species and segregated SrO, owing to the fact that generation of manganese species in particular, Mn^{2+} is depressed under anodic polarization conditions. This would lead to Cr deposition and $SrCrO_4$ formation in the bulk of the electrode. The high Sr segregation at the electrode/electrolyte interface region would lead to the substantially higher reaction activity between the segregated SrO and gaseous Cr species. This is supported by the observations that in the presence of the interconnect, a high polarization current of 500 mA cm^{-2} significantly accelerates Cr deposition particularly at the electrode/electrolyte interface regions under the rib of the interconnect. The degree of chromium deposition on the YSZ electrolyte surface is significantly higher than that under a low current of 200 mA cm^{-2}, indicated by the significant grain

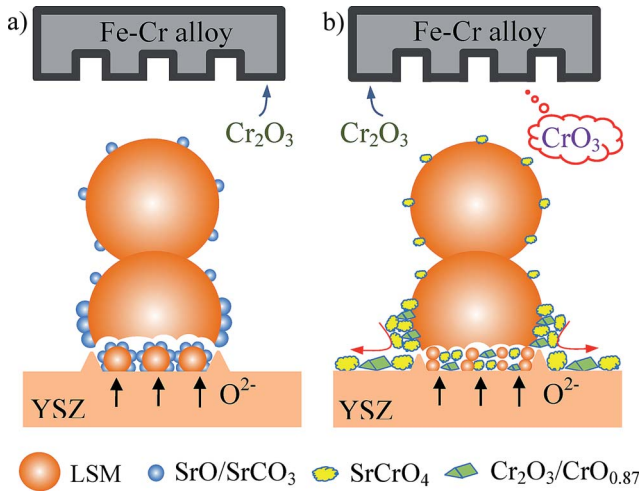

Fig. 10 Schemes of Cr deposition on LSM oxygen electrodes under SOEC operating conditions. (a) LSM nanoparticle formation at the electrode/electrolyte interface and accelerated SrO segregation from the bulk to the LSM surface under anodic polarization; (b) $Co_2O_3/CrO_{0.87}$ and $SrCrO_4$ formation on the LSM surface, at the electrode/electrolyte interface, and on the YSZ electrolyte surface. The red arrows indicate the migration of SrO/$SrCO_3$ from the LSM surface to the YSZ electrolyte surface.

growth of deposited particles on the YSZ electrolyte surface (Fig. 5a and b). The high activity between the Sr and Cr could also lead to the spread of Sr species from the LSM electrode to the YSZ surface. The high mobility of SrO in the presence of Cr has been reported in the case of LSCF and LSC oxygen electrode,[26,41,42] evident by the long-range transport of Sr from electrode bulk to the outermost surface. This is supported by high Cr deposition and significant $SrCrO_4$ formation on the YSZ electrolyte surface between the contact rings and on the LSM electrode inner surface (Fig. 4 and 7). The accelerated migration and segregation of SrO from the bulk to the free surface and subsequent reaction between SrO and gaseous Cr species based on the nucleation theory[19] are summarized below and schematically shown in Fig. 10b.

Sr segregation:

$$La_{0.8}Sr_{0.2}MnO_{3+\delta} \rightarrow La_{0.8}Sr_{0.2-x}MnO_{3+\delta} + xSrO \quad (1)$$

Cr deposition *via* nucleation and grain growth route:

$$SrO + CrO_3 \rightarrow Cr\text{–}Sr\text{–}O_x \text{ (nuclei)} \quad (2)$$

$$Cr\text{–}Sr\text{–}O + CrO_3 \rightarrow CrO_y + Cr_2O_3 \quad (3)$$

$$Cr\text{–}Sr\text{–}O + SrO + CrO_3 \rightarrow SrCrO_4 \quad (4)$$

The segregated Sr species could also exist as $SrCO_3$ as indicated by the XPS results (Fig. 9c). The excess segregation of Sr could also result in the partial decomposition of LSM and this appears to be supported by the shift of $Mn2p_{3/2}$ to

a lower BE of 639.5 eV, an indication of the presence of MnO on the YSZ surface under the rib of the interconnect after polarization at 500 mA cm^{-2} and 800 °C for 20 h in the presence of the Fe–Cr interconnect.

5. Conclusions

Cr deposition and poisoning of LSM oxygen electrodes are investigated in detail for the first time under anodic operating conditions. The presence of a chromia-forming alloy metallic interconnect significantly degrades and poisons the electrocatalytic activity of LSM oxygen electrodes for the O_2 oxidation reaction, accelerating the delamination of the electrodes. Cr deposition occurs in the LSM electrode bulk and in particular on the YSZ electrolyte surface and on LSM electrode inner surface close to the electrode/electrolyte interface. The results show the formation of Cr, $CrO_{0.87}$, Cr_2O_3, Cr_2O_5, and $SrCrO_4$ on the YSZ electrolyte surface, within the contact rings and on the LSM inner surface. Very different from the predominant formation of $(Cr,Mn)_3O_4$ spinels for the LSM electrodes under the SOFC operating conditions, the $(Cr,Mn)_3O_4$ spinel phase could not be found on the LSM oxygen electrodes under SOEC operating conditions. The fundamental reason for the observation of $SrCrO_4$ formation instead of $(CrMn)_3O_4$ on the LSM electrode under SOEC operating conditions is that anodic polarization promotes Sr segregation and depresses Mn segregation. Thus, under SOEC operating conditions, the nucleation agent for Cr deposition on LSM electrodes is the segregated SrO or $SrCO_3$ and not the manganese species, Mn^{2+}, generated under polarization conditions. Due to the high activity of gaseous Cr species with segregated Sr species, the segregated Sr species could be highly mobile and readily spread to the YSZ electrolyte surface. This may be the reason for significant Cr deposition and formation of $SrCrO_4$ on the YSZ electrolyte surface area between the contact rings.

Finally, the present study also provides clear evidence that the delamination or failure of LSM oxygen electrodes is primarily due to the disintegration or breaking of LSM particles attached to the YSZ electrolyte surface, forming nanoparticles at the interface under anodic polarization conditions as proposed early,[12,13] and not by the formation of highly resistive $La_2Zr_2O_7$ at the electrode/electrolyte interface.[11] This is supported by the correlation between the nanoparticle formation and easy delamination of the LSM electrodes under the rib of the interconnect as compared to that under the channel of the interconnect.

Acknowledgements

The project is supported by the Curtin University Research Fellowship, Australian Research Council (LP110200281), Australia, and National Natural Science Foundation of China (U1134001). The authors acknowledge the facilities, scientific and technical assistance of the Curtin University Electron Microscope Facility, the Australian Microscopy & Microanalysis Research Facility at the Centre for Microscopy, Characterisation & Analysis, The University of Western Australia, both of which are funded by the University, State and Commonwealth Governments, and the WA X-Ray Surface Analysis Facility, funded by the Australian Research Council LIEF grant (LE120100026). The authors also thank Dr Catherine Kealley, Curtin University, for the XRD data analysis.

References

1 J. Schefold, A. Brisse, M. Zahid, J. P. Ouweltjes and J. U. Nielsen, *ECS Trans.*, 2011, **35**, 2915–2927.
2 N. Q. Minh, *ECS Trans.*, 2011, **35**, 2897–2904.
3 X. Zhang, J. E. O'Brien, R. C. O'Brien and G. K. Housley, *J. Power Sources*, 2013, **242**, 566–574.
4 S. Elangovan, J. Hartvigsen, D. Larsen, I. Bay and F. Zhao, *ECS Trans.*, 2011, **35**, 2875–2882.
5 A. Momma, T. Kato, Y. Kaga and S. Nagata, *J. Ceram. Soc. Jpn.*, 1997, **105**, 369–373.
6 J. R. Mawdsley, J. D. Carter, A. J. Kropf, B. Yildiz and V. A. Maroni, *Int. J. Hydrog. Energy*, 2009, **34**, 4198–4207.
7 G. A. Hughes, K. Yakal-Kremski and S. A. Barnett, *Phys. Chem. Chem. Phys.*, 2013, **15**, 17257–17262.
8 A. V. Virkar, *Int. J. Hydrog. Energy*, 2010, **35**, 9527–9543.
9 R. Knibbe, M. L. Traulsen, A. Hauch, S. D. Ebbesen and M. Mogensen, *J. Electrochem. Soc.*, 2010, **157**, B1209–B1217.
10 J. Kim, H.-I. Ji, H. P. Dasari, D. Shin, H. Song, J.-H. Lee, B.-K. Kim, H.-J. Je, H.-W. Lee and K. J. Yoon, *Int. J. Hydrogen Energy*, 2013, **38**, 1225–1235.
11 M. Keane, M. K. Mahapatra, A. Verma and P. Singh, *Int. J. Hydrogen Energy*, 2012, **37**, 16776–16785.
12 K. Chen, N. Ai and S. P. Jiang, *Int. J. Hydrogen Energy*, 2012, **37**, 10517–10525.
13 K. F. Chen and S. P. Jiang, *Int. J. Hydrog. Energy*, 2011, **36**, 10541–10549.
14 F. Tietz, D. Sebold, A. Brisse and J. Schefold, *J. Power Sources*, 2013, **223**, 129–135.
15 D. The, S. Grieshammer, M. Schroeder, M. Martin, M. Al Daroukh, F. Tietz, J. Schefold and A. Brisse, *J. Power Sources*, 2015, **275**, 901–911.
16 H. Fan, M. Keane, P. Singh and M. Han, *J. Power Sources*, 2014, **268**, 634–639.
17 S. J. Kim and G. M. Choi, *Solid State Ionics*, 2014, **262**, 303–306.
18 W. Z. Zhu and S. C. Deevi, *Mater. Res. Bull.*, 2003, **38**, 957–972.
19 S. P. Jiang and X. B. Chen, *Int. J. Hydrog. Energy*, 2014, **39**, 505–531.
20 S. P. S. Badwal, R. Deller, K. Foger, Y. Ramprakash and J. P. Zhang, *Solid State Ionics*, 1997, **99**, 297–310.
21 S. P. Jiang, J. P. Zhang, L. Apateanu and K. Foger, *J. Electrochem. Soc.*, 2000, **147**, 4013–4022.
22 T. Horita, Y. P. Xiong, M. Yoshinaga, H. Kishimoto, K. Yamaji, M. E. Brito and H. Yokokawa, *Electrochem. Solid State Lett.*, 2009, **12**, B146–B149.
23 X. Zhang, J. E. O'Brien, R. C. O'Brien, J. J. Hartvigsen, G. Tao and G. K. Housley, *Int. J. Hydrogen Energy*, 2013, **38**, 20–28.
24 J. W. Fergus, *Int. J. Hydrog. Energy*, 2007, **32**, 3664–3671.
25 B. Wei, K. F. Chen, L. Zhao, Z. Lu and S. P. Jiang, *Phys. Chem. Chem. Phys.*, 2015, **17**, 1601–1609.
26 V. I. Sharma and B. Yildiz, *J. Electrochem. Soc.*, 2010, **157**, B441–B448.
27 L. Zhao, S. Amarasinghe and S. P. Jiang, *Electrochem. Commun.*, 2013, **37**, 84–87.
28 A. Mitterdorfer and L. J. Gauckler, *Solid State Ionics*, 1998, **111**, 185–218.
29 S. P. Jiang and W. Wang, *Electrochem. Solid State Lett.*, 2005, **8**, A115–A118.

30 X. B. Chen, L. Zhang, E. J. Liu and S. P. Jiang, *Int. J. Hydrog. Energy*, 2011, **36**, 805–821.
31 S. P. Jiang, J. P. Zhang, Y. Ramprakash, D. Milosevic and K. Wilshier, *J. Mater. Sci.*, 2000, **35**, 2735–2741.
32 J. Mizusaki, H. Tagawa, K. Naraya and T. Sasamoto, *Solid State Ionics*, 1991, **49**, 111–118.
33 U. Scharf, H. Schneider, A. Baiker and A. Wokaun, *J. Catal.*, 1994, **145**, 464–478.
34 P. Parhi and V. Manivannan, *J. Alloys Compd.*, 2009, **469**, 558–564.
35 T. L. Daulton, B. J. Little, K. Lowe and J. Jones-Meehan, *Journal of Microbiological Methods*, 2002, **50**, 39–54.
36 C. Knöfel, H.-J. Wang, K. T. S. Thydén and M. Mogensen, *Solid State Ionics*, 2011, **195**, 36–42.
37 Q.-H. Wu, M. Liu and W. Jaegermann, *Mater. Lett.*, 2005, **59**, 1980–1983.
38 F. Liu and J. Jia, *Tribol Lett*, 2013, **49**, 281–290.
39 E. Mutoro, E. J. Crumlin, M. D. Biegalski, H. M. Christen and Y. Shao-Horn, *Energy & Environmental Science*, 2011, **4**, 3689–3696.
40 E. Z. Kurmaev, M. A. Korotin, V. R. Galakhov, L. D. Finkelstein, E. I. Zabolotzky, N. N. Efremova, N. I. Lobachevskaya, S. Stadler, D. L. Ederer, T. A. Callcott, L. Zhou, A. Moewes, S. Bartkowski, M. Neumann, J. Matsuno, T. Mizokawa, A. Fujimori and J. Mitchell, *Physical Review B*, 1999, **59**, 12799–12806.
41 Y. Wang and Y. Ohtsuka, *Applied Catalysis A: General*, 2001, **219**, 183–193.
42 W. Wang and S. P. Jiang, *J. Solid State Electrochem.*, 2004, **8**, 914–922.
43 W. S. Wang, Y. Y. Huang, S. W. Jung, J. M. Vohs and R. J. Gorte, *J. Electrochem. Soc.*, 2006, **153**, A2066–A2070.
44 X. B. Chen, L. Zhang, E. Liu and S. P. Jiang, *Int. J. Hydrogen Energy*, 2011, **36**, 805–821.
45 T. Horita, Y. P. Xiong, H. Kishimoto, K. Yamaji, M. E. Brito and H. Yokokawa, *J. Electrochem. Soc.*, 2010, **157**, B614–B620.
46 N. Caillol, M. Pijolat and E. Siebert, *Appl. Surf. Sci.*, 2007, **253**, 4641–4648.
47 S. P. Jiang and J. G. Love, *Solid State Ionics*, 2001, **138**, 183–190.
48 S. P. Jiang, *J. Mater. Sci.*, 2008, **43**, 6799–6833.
49 H. P. Ding, A. V. Virkar, M. L. Liu and F. Liu, *Phys. Chem. Chem. Phys.*, 2013, **15**, 489–496.
50 L. Zhao, J. Drennan, C. Kong, S. Amarasinghe and S. P. Jiang, *Journal of Materials Chemistry A*, 2014, **2**, 11114–11123.
51 D. Oh, D. Gostovic and E. D. Wachsman, *J. Mater. Res.*, 2012, **27**, 1992–1999.
52 W. Lee, J. W. Han, Y. Chen, Z. Cai and B. Yildiz, *J. Am. Chem. Soc.*, 2013, **135**, 7909–7925.
53 M. Fister, *Appl. Phys. Lett.*, 2008, **93**, 151904.
54 M. Backhaus-Ricoult, K. Adib, T. S. Clair, B. Luerssen, L. Gregoratti and A. Barinov, *Solid State Ionics*, 2008, **179**, 891–895.
55 A.-K. Huber, M. Falk, M. Rohnke, B. Luerssen, L. Gregoratti, M. Amati and J. Janek, *Phys. Chem. Chem. Phys.*, 2012, **14**, 751–758.
56 S. Carter, A. Selcuk, R. J. Chater, J. Kajda, J. A. Kilner and B. C. H. Steele, *Solid State Ionics*, 1992, **53–6**, 597–605.